

SCIENTIFIC REPORTS



OPEN

Multifunctional Fe₃O₄ @ Au core/shell nanostars: a unique platform for multimode imaging and photothermal therapy of tumors

Received: 19 February 2016

Accepted: 02 June 2016

Published: 21 June 2016

Yong Hu¹, Ruizhi Wang², Shige Wang³, Ling Ding¹, Jingchao Li¹, Yu Luo¹, Xiaolin Wang², Mingwu Shen¹ & Xiangyang Shi¹

We herein report the development of multifunctional folic acid (FA)-targeted Fe₃O₄ @ Au nanostars (NSs) for targeted multi-mode magnetic resonance (MR)/computed tomography (CT)/photoacoustic (PA) imaging and photothermal therapy (PTT) of tumors. In this present work, citric acid-stabilized Fe₃O₄/Ag composite nanoparticles prepared by a mild reduction route were utilized as seeds and exposed to the Au growth solution to induce the formation of Fe₃O₄ @ Au core/shell NSs. Followed by successive decoration of thiolated polyethyleneimine (PEI-SH), FA via a polyethylene glycol spacer, and acetylation of the residual PEI amines, multifunctional Fe₃O₄ @ Au NSs were formed. The designed multifunctional NSs possess excellent colloidal stability, good cytocompatibility in a given concentration range, and specific recognition to cancer cells overexpressing FA receptors. Due to co-existence of Fe₃O₄ core and star-shaped Au shell, the NSs can be used for MR and CT imaging of tumors, respectively. Likewise, the near infrared plasmonic absorption feature also enables the NSs to be used for PA imaging and PTT of tumors. Our study clearly demonstrates a unique theranostic nanoplatform that can be used for high performance multi-mode imaging-guided PTT of tumors, which may be extendable for theranostics of different diseases in translational medicine.

Molecular imaging (MI) provides the means to study *in vivo* processes that have tremendous potential applications in biomedical research and clinical diagnosis^{1–3}. Although each modality imaging has its own merits, no single technique is capable of giving complete information in disease diagnosis due to its intrinsic drawbacks in terms of sensitivity, spatial and temporal resolution, multiplexing capability, and response time^{4–6}. Among many types of MI technologies, magnetic resonance (MR) imaging has been generally considered as one of the most powerful noninvasive imaging techniques owing to its great spatial resolution and tomographic capabilities^{7–10}. Computed tomography (CT) affords better spatial and density resolution than other imaging techniques^{11,12}. In addition, photoacoustic (PA) imaging is a non-invasive imaging technique with high resolution and provides fast, quantitative, volumetric measurement with deep tissue penetration capability^{13,14}. However, the spatial resolution of MR imaging is lower than that of CT imaging, while the soft tissue contrast of CT imaging is lower than that of MR imaging. Meanwhile, PA imaging is still at the phases of basic research for now and have not been widely used in clinical applications. Therefore, combination of these three diagnostic modalities is expected to be able to overcome some serious restrictions encountered by each MI technique when used alone, leading to much more accurate disease diagnosis, in particular cancer. Besides precision cancer diagnosis, it is desirable to perform simultaneous treatment of cancer. Among many different cancer therapy approaches, photothermal therapy (PTT) has attracted great interest in recent years due to the advantage that the light-induced heating, as a non-invasive strategy, is able to ablate cancerous cells without damaging surrounding normal tissues^{15–18}.

¹State Key Laboratory for Modification of Chemical Fibers and Polymer Materials, College of Chemistry, Chemical Engineering and Biotechnology, Donghua University, Shanghai 201620, People's Republic of China. ²Shanghai Institute of Medical Imaging, Department of Interventional Radiology, Zhongshan Hospital, Fudan University, Shanghai 200032, People's Republic of China. ³College of Science, University of Shanghai for Science & Technology, Shanghai 200093, People's Republic of China. Correspondence and requests for materials should be addressed to X.W. (email: xlwang-shmu@vip.sina.com) or M.S. (email: mwshen@dhu.edu.cn) or X.S. (email: xshi@dhu.edu.cn)

Recent advances in nanotechnology exhibit vast potential to generate various platforms that can be used for cancer theranostics^{19–21}. Among the used nanomaterials, iron oxide (Fe_3O_4) nanoparticles (NPs), due to their ability to shorten the T_2 relaxation time of their surrounding water protons and biocompatibility, can be used as T_2 negative contrast agents for MR imaging^{10,22}. On the other hand, gold (Au) NPs, owing to the higher atomic number of Au than that of iodine for iodinated CT contrast agents (e.g., Omnipaque), have been explored as CT imaging agents^{23,24}. For accurate dual mode MR/CT imaging applications, $\text{Fe}_3\text{O}_4/\text{Au}$ composite nanoparticles (CNPs) has been designed^{25,26}. For example, Cai *et al.* synthesized $\text{Fe}_3\text{O}_4/\text{Au}$ CNPs with the assistance of dendrimers that can be used for MR/CT imaging of animal organs/tissues²⁵ and tumors *in vivo*²⁷. Zhu *et al.*²⁰ reported the preparation of Au- Fe_3O_4 heterostructured NPs for dual mode MR/CT imaging of liver in an intravital model. It is known that Au NPs with a particular shape such as nanostars (NSs)^{28–30}, nanorods^{31–33}, nanoflowers^{21,34}, or nanocages^{35,36} are able to exhibit strong localized surface plasmon resonance (SPR) absorbance in near infrared (NIR) region for PTT of cancer cells^{15,31,37,38}. Furthermore, Au NPs with these specific shapes can be used for PA imaging through the absorption of a pulsed light and the detection of the resultant ultrasonic (US) wave profile by special transducer^{13,14}. For example, Nie *et al.*¹³ demonstrated that gold NSs were able to be simultaneously used for PTT and PA imaging of tumors. Accordingly, in order to develop a unique platform that can be used for simultaneous multimode imaging and PTT of tumors, it is desirable to integrate Fe_3O_4 NPs with specific shaped Au NPs.

In our previous study, we have shown that $\text{Fe}_3\text{O}_4 @ \text{Au}$ NSs can be formed by exposing $\text{Fe}_3\text{O}_4 @ \text{Ag}$ seed particles to Au growth solution, and can be functionalized *via* polyethyleneimine (PEI)-mediated covalent conjugation reaction for *in vivo* MR/CT imaging and PTT of tumors *via* intratumoral administration of the particles³⁹. However, this study was limited to use hyaluronic acid as a targeting ligand and to just use intratumoral injection as an administration route. Furthermore, the PA imaging potential of the developed $\text{Fe}_3\text{O}_4 @ \text{Au}$ NSs has not been explored. Therefore, it is still challengeable to develop multifunctional $\text{Fe}_3\text{O}_4 @ \text{Au}$ NSs using different approaches for multimode imaging-guided PTT of tumors.

In this present work, a unique multifunctional nanoplatform based on folic acid (FA)-modified $\text{Fe}_3\text{O}_4 @ \text{Au}$ NSs were designed for tri-mode MR/CT/PA imaging and PTT of tumors. $\text{Fe}_3\text{O}_4/\text{Ag}$ composite particles were first synthesized by sodium borohydride (NaBH_4) reduction of Ag(I) ions on the surface of citric acid (CA)-coated Fe_3O_4 NPs formed *via* a mild reduction route according to the literature^{10,40,41}. The as-prepared $\text{Fe}_3\text{O}_4/\text{Ag}$ composite particles were utilized as seeds and exposed to the aqueous Au growth solution to induce the formation of $\text{Fe}_3\text{O}_4 @ \text{Au}$ NSs. Thereafter, the obtained $\text{Fe}_3\text{O}_4 @ \text{Au}$ NSs were decorated with thiolated PEI (PEI-SH) *via* Au-S bond. Finally, the PEI-coated $\text{Fe}_3\text{O}_4 @ \text{Au}$ NSs were sequentially conjugated with FA through a polyethylene glycol (PEG) spacer *via* the PEI amine-enabled conjugation chemistry. This was followed by acetylation of the remaining PEI amines (Fig. 1a). The formed multifunctional FA-modified $\text{Fe}_3\text{O}_4 @ \text{Au}$ ($\text{Fe}_3\text{O}_4 @ \text{Au}$ -PEI-Ac-PEG-FA) NSs were exhaustively characterized. Their hemocompatibility, cytocompatibility, specific recognition to FA receptor (FAR)-overexpressing cancer cells, and potential for multi-mode MR/CT/PA imaging and PTT of tumors were evaluated in detail.

Results

Formation and characterization of the $\text{Fe}_3\text{O}_4 @ \text{Au}$ -PEI-Ac-PEG-FA NSs. According to our previous work¹⁰, Fe_3O_4 NPs were synthesized *via* a mild reduction route for targeted *in vivo* MR imaging of tumors. This facile mild reduction strategy enabled the generation of Fe_3O_4 NPs with ultrahigh r_2 relaxivity. In this study, by virtue of the same approach, we synthesized CA-stabilized Fe_3O_4 NPs ($\text{Fe}_3\text{O}_4 @ \text{CA}$) and further created $\text{Fe}_3\text{O}_4/\text{Ag}$ seed particles by NaBH_4 reduction of Ag(I) in the presence of the $\text{Fe}_3\text{O}_4 @ \text{CA}$ NPs according to the literature⁴¹. The formed $\text{Fe}_3\text{O}_4/\text{Ag}$ seed particles are quite uniform in size (Supplementary Fig. S1a) with an average size of 9.3 nm (Fig. S1b). The apparent absorption peak at 400 nm can be ascribed to the SPR peak of Ag component (Fig. S1c), confirming the formation of $\text{Fe}_3\text{O}_4/\text{Ag}$ seed particles. Likewise, the existence of both Ag and Fe in the energy dispersive spectrum (Fig. S1d) also confirmed the formation of the $\text{Fe}_3\text{O}_4/\text{Ag}$ seed particles. The composition of the $\text{Fe}_3\text{O}_4/\text{Ag}$ seed particles was further quantified using ICP-OES and the molar ratio of $\text{Fe}_3\text{O}_4/\text{Ag}$ was measured to be 1.9:1.

By exposing the $\text{Fe}_3\text{O}_4/\text{Ag}$ seeds to the Au growth solution, star-shaped $\text{Fe}_3\text{O}_4 @ \text{Au}$ were generated. The NIR-absorbance feature of the NSs was validated by UV-vis spectroscopy (Supplementary Fig. S2). By optimizing the concentration of the chemicals, $\text{Fe}_3\text{O}_4/\text{Au}$ NSs with a desirable NIR-absorption feature were obtained using an Au growth solution containing 2.4 mM HAuCl_4 , 0.08 mM AgNO_3 , 5.2 mM AA. The formed CTAB-stabilized $\text{Fe}_3\text{O}_4 @ \text{Au}$ NSs display unique star-shaped spikes with a narrow size distribution (Supplementary Fig. S3). In order to make the NSs be functionalized, the NSs were copiously washed to remove the surfactant CTAB, and modified with PEI-SH *via* Au-S bond formation according to our previous work³⁹. The PEI-SH synthesized was characterized by ¹H NMR to have 15.3 thiol groups per PEI (Supplementary Fig. S4a). The generated PEI-stabilized $\text{Fe}_3\text{O}_4 @ \text{Au}$ ($\text{Fe}_3\text{O}_4 @ \text{Au}$ -PEI) NSs with a large amount of primary amines were further grafted with COOH-PEG-FA, which was characterized to have 0.8 FA moieties per PEG by ¹H NMR (Fig. S4b). This FA modification onto the NSs *via* a PEG spacer is expected to endow the NSs with high affinity to cancer cells overexpressing FAR¹⁹. Finally, the synthesized $\text{Fe}_3\text{O}_4 @ \text{Au}$ -PEI-PEG-FA NSs were subjected to an acetylation reaction to neutralize the residual PEI surface amines in order to improve their cytocompatibility⁴².

Zeta potential and hydrodynamic size of NSs produced in each step were measured to confirm their surface modification (Supplementary Table S1). Clearly, $\text{Fe}_3\text{O}_4 @ \text{Au}$ -PEI NSs possess a quite positive surface potential (+31.4 mV) due to the surface modification of PEI with a large amount of amines. After the successive modification of COOH-PEG-FA and acetylation reaction, the surface potentials of the $\text{Fe}_3\text{O}_4 @ \text{Au}$ -PEI-PEG-FA and $\text{Fe}_3\text{O}_4 @ \text{Au}$ -PEI-Ac-PEG-FA NSs were measured to be +28.3 and +14.4 mV, respectively. The decreased surface potential for both NSs validated the success of the modification of COOH-PEG-FA and acetylation reaction when compared to that of the $\text{Fe}_3\text{O}_4 @ \text{Au}$ -PEI NSs. Likewise, the hydrodynamic sizes of the $\text{Fe}_3\text{O}_4 @ \text{Au}$ -PEI-PEG-FA

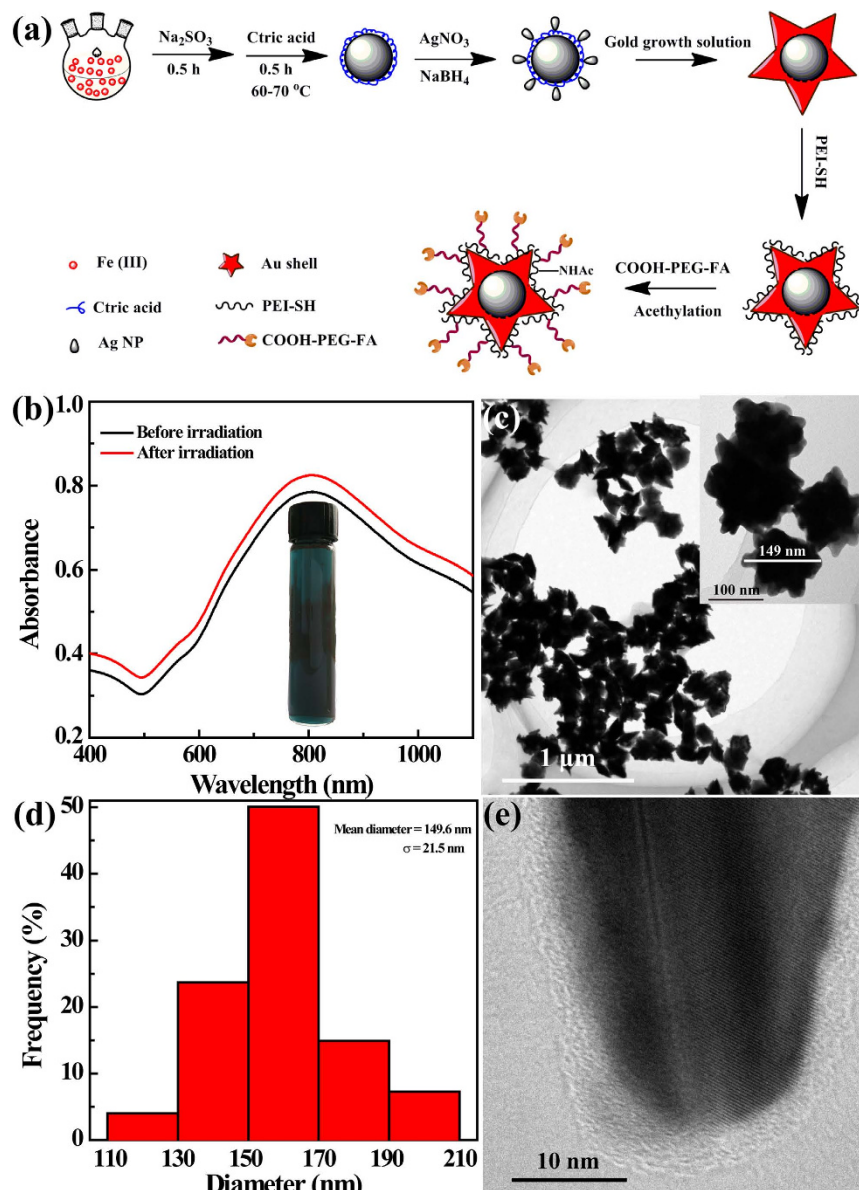


Figure 1. Synthesis and characterization of the $\text{Fe}_3\text{O}_4@ \text{Au-PEI.Ac-PEG-FA}$ NSs. (a) Schematic representation of the synthesis of the $\text{Fe}_3\text{O}_4@ \text{Au-PEI.Ac-PEG-FA}$ NSs. (b) UV-vis spectra of the aqueous solution of $\text{Fe}_3\text{O}_4@ \text{Au-PEI.Ac-PEG-FA}$ NSs before and after laser irradiation (inset shows the digital photo of the $\text{Fe}_3\text{O}_4@ \text{Au-PEI.Ac-PEG-FA}$ NSs in aqueous solution). (c) TEM image (inset is the high magnification TEM image), (d) size distribution histogram, and (e) high-resolution TEM image (only an Au spike is shown) of the $\text{Fe}_3\text{O}_4@ \text{Au-PEI.Ac-PEG-FA}$ NSs.

(226.1 nm) and $\text{Fe}_3\text{O}_4@ \text{Au-PEI.Ac-PEG-FA}$ (224.2 nm) NSs are larger than that of the $\text{Fe}_3\text{O}_4@ \text{Au-PEI}$ NSs (211.3 nm), suggesting the successful surface modification of the NSs. Additionally, the hydrodynamic size of the final $\text{Fe}_3\text{O}_4@ \text{Au-PEI.Ac-PEG-FA}$ NSs was also occasionally measured within a time period of 15 days (Supplementary Fig. S5). We show that the hydrodynamic size of NSs does not display any obvious fluctuation, suggesting their laudable colloidal stability. Moreover, the long-term colloidal stability of the $\text{Fe}_3\text{O}_4@ \text{Au-PEI.Ac-PEG-FA}$ NSs was evaluated by exposing them to different media (water, PBS, and DMEM containing 10% FBS, respectively) for at least one month (Fig. S5 and inset). The particles do not precipitate, further confirming their long-term colloidal stability.

To quantify the conjugated PEI and COOH-PEG-FA on the surface of the $\text{Fe}_3\text{O}_4@ \text{Au}$ NSs, TGA were performed (Supplementary Fig. S6). At 700 °C, the PEI coating results in a weight loss of 4.8% for the $\text{Fe}_3\text{O}_4@ \text{Au-PEI}$ NSs, when compared with the CTAB-free $\text{Fe}_3\text{O}_4@ \text{Au}$ NSs. Further conjugation of COOH-PEG-FA affords the $\text{Fe}_3\text{O}_4@ \text{Au-PEI-PEG-FA}$ NSs with an increased weight loss of 12.4%. Therefore, the modified COOH-PEG-FA onto the NSs was deduced to be 7.6%.

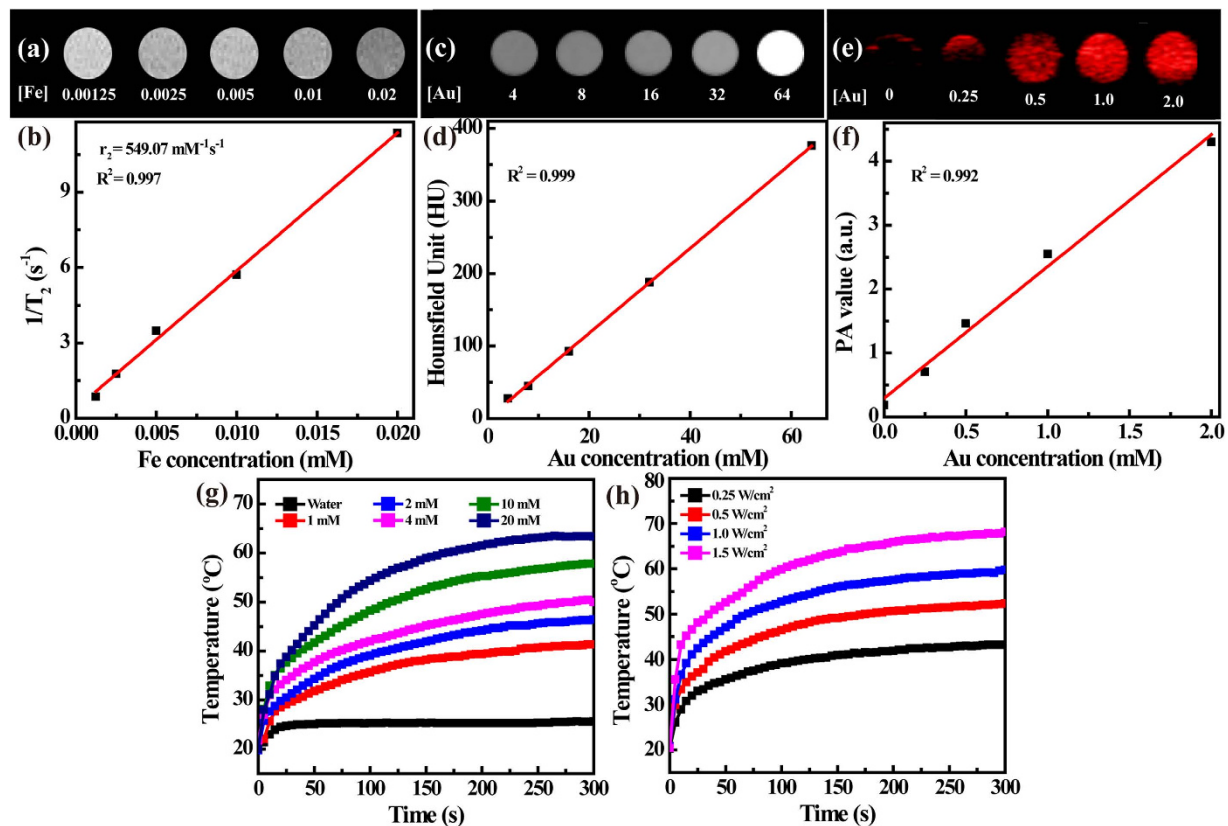


Figure 2. MR relaxometry, X-ray attenuation property, photoacoustic property and photothermal performance of the $\text{Fe}_3\text{O}_4@ \text{Au-PEI.Ac-PEG-FA NSs}$. (a) T_2 -weighted MR images and (b) linear fitting of $1/T_2$ of the $\text{Fe}_3\text{O}_4@ \text{Au-PEI.Ac-PEG-FA NSs}$ as a function of Fe concentration. (c) CT images and (d) linear fitting of CT values (HU) of the $\text{Fe}_3\text{O}_4@ \text{Au-PEI.Ac-PEG-FA NSs}$ at an Au concentration of 4, 8, 16, 32, and 64 mM, respectively. (e) PA images and (f) linear fitting of PA values of the $\text{Fe}_3\text{O}_4@ \text{Au-PEI.Ac-PEG-FA NSs}$ at an Au concentration of 0, 0.25, 0.5, 1.0, and 2.0 mM, respectively. (g) Temperature change of water and water containing the $\text{Fe}_3\text{O}_4@ \text{Au-PEI.Ac-PEG-FA NSs}$ at varying Au concentrations (1, 2, 4, 10, and 20 mM, respectively) under an 808 nm laser irradiation with the same power density of 1.0 W/cm^2 as a function of irradiation time. (h) Temperature change of a water solution containing the $\text{Fe}_3\text{O}_4@ \text{Au-PEI.Ac-PEG-FA NSs}$ at an Au concentration of 10 mM under an 808 nm laser irradiation with different power densities ($0.25, 0.5, 1.0,$ and 1.5 W/cm^2 , respectively) as a function of irradiation time.

The optical property of the $\text{Fe}_3\text{O}_4@ \text{Au-PEI.Ac-PEG-FA NSs}$ was investigated by UV-vis spectroscopy (Fig. 1b). The dark blue color of NSs in aqueous solution was ascribed to the star-shaped Au shell coating on the particle surface (Fig. 1b, inset). An obvious SPR peak in the NIR region at 810 nm can be clearly seen, and the NIR absorption feature does not show obvious changes even when the NSs were irradiated with an 808 nm laser at 2.0 W/cm^2 for 20 min. This suggests that the NSs display an excellent photothermal stability and also a great potential to use them for PTT of tumors. TEM was employed to observe the morphology and size of the $\text{Fe}_3\text{O}_4@ \text{Au-PEI.Ac-PEG-FA NSs}$ (Fig. 1c–e). We can clearly see that the NSs with Au shell coating onto the surface of Fe_3O_4 NPs possess well-defined star shape and a quite uniform size distribution (Fig. 1c). By measuring two maximal margins of the NSs, the mean diameter of NSs was estimated to be $149.6 \pm 21.5 \text{ nm}$ (Fig. 1d). As depicted in Fig. 1e, high-resolution TEM image reveals the clear lattices of the spike-like Au shell crystals and also a dense polymer coating on the outer surface of the NSs, which is relevant to the PEI modification and COOH-PEG-FA grafting. The elemental composition of Fe and Au in the $\text{Fe}_3\text{O}_4@ \text{Au-PEI.Ac-PEG-FA NSs}$ was quantified by ICP-OES, and the Fe/Au molar ratio was measured to be 1:53.4.

MR and CT phantom studies. Fe_3O_4 NPs are generally used as MR contrast agents because of their capacity to shorten the T_2 relaxation time of their surrounding water protons. From T_2 -weighted MR imaging, we can find that the generated $\text{Fe}_3\text{O}_4@ \text{Au-PEI.Ac-PEG-FA NSs}$ can gradually decrease the MR signal intensity of water with the increase of Fe concentration (Fig. 2a). By linearly fitting the T_2 relaxation rate ($1/T_2$) versus Fe concentration, the r_2 relaxivity of the NSs was calculated to be $549.07 \text{ mM}^{-1} \text{ s}^{-1}$ (Fig. 2b). The ultrahigh r_2 relaxivity of the NSs should be due to the nature of the mild reduction approach used to synthesize Fe_3O_4 NPs, in agreement with the literature¹⁰. It seems that the Au shell coating does not appreciably affect the accessibility of water protons to the inner Fe_3O_4 NPs, due largely to the interstitial spaces between each Au spikes of the NSs.

On the other hand, CT phantom studies of the $\text{Fe}_3\text{O}_4@ \text{Au-PEI.Ac-PEG-FA NSs}$ were carried out to explore their potential for CT imaging (Fig. 2c). It can be clearly seen that, with the increase of Au concentration, the CT

image of the NSs-containing aqueous suspension gradually brightens, well matching the quantitative measurement of their CT value (HU) versus Au concentration (Fig. 2d).

Photoacoustic property and photothermal performance of the Fe₃O₄@Au-PEI.Ac-PEG-FA NSs. To explore the feasibility to employ the Fe₃O₄@Au-PEI.Ac-PEG-FA NSs for PA imaging, PA phantom studies were first carried out (Fig. 2e). Clearly, with the Au concentration of the NSs, the PA signal intensity gradually enhances, which correlates well with the quantitative PA signal intensity change versus Au concentration (Fig. 2f).

The photothermal behavior of the Fe₃O₄@Au-PEI.Ac-PEG-FA NSs was next investigated to unleash their potential to be used for PTT of tumors. The temperature variation of the the NSs-containing aqueous solution versus Au concentration (1–20 mM) was continuously monitored in real time after exposure to an 808 nm laser at 1.0 W/cm² for 300 s (Fig. 2g). Clearly, the NSs are able to induce a positive temperature enhancement in a concentration-dependent manner. The temperature of the NS suspension can reach 63.3 °C at the Au concentration of 20 mM. For comparison, laser irradiation of pure water under the same conditions does not afford obvious temperature increase. At a given Au concentration of 10 mM, the NS suspension irradiated under an 808 nm laser at different output power densities (0.25–1.5 W/cm²) for 300 s was also monitored to check the temperature change (Fig. 2h). It is evident that the NSs are able to generate heat in a laser output power density-dependent manner. The temperature of the NS suspension rises to 68.5 °C at the highest laser output power density (1.5 W/cm²). These results indicate that the synthesized Fe₃O₄@Au-PEI.Ac-PEG-FA NSs were able to transform NIR laser into heat rapidly under laser irradiation. The photothermal conversion efficiency (η) of the NSs was calculated according to the literature^{43,44}. Details can be seen in Supplementary information. The η of the NSs was calculated to be 88.9%, which is prominently higher than that of other major PTT agents^{43–46}.

Hemolytic and cytotoxicity assays. For biomedical applications, it is vital to evaluate the hemocompatibility and cytocompatibility of the prepared Fe₃O₄@Au-PEI.Ac-PEG-FA NSs. The hemolytic activity of the NSs was evaluated by hemolytic assay (Supplementary Fig. S8a). When compared to the positive water control, where obvious hemolytic behavior occurs, NSs at different Au concentrations do not display appreciable hemolysis effect, similar to the negative PBS control (inset of Fig. S8a). The hemolysis percentages of HRBCs exposed to NS solution at different Au concentrations were calculated to be 0.39%, 1.79%, 2.51%, and 4.39%, respectively, which are all less than the threshold value of 5%, indicating their excellent hemocompatibility in the given Au concentration range^{47,48}.

The cytocompatibility of the Fe₃O₄@Au-PEI.Ac-PEG-FA NSs was assessed by MTT assay of viability of HeLa cell (Fig. S8b). Apparently, after cultivation of HeLa cells with NSs at an Au concentration of 0.2, 0.4, 0.8, 1.5, and 2.0 mM, respectively, for 24 h, the cell viability still keeps larger than 80%, suggesting their negligible cytotoxicity^{19,47}. The cytocompatibility of the NSs was further validated by observing the morphology of HeLa cells (Supplementary Fig. S9). Clearly, the morphology of HeLa cells after treatment with the NSs in the given Au concentration range (0.2–2.0 mM) (Fig. S9b–f) is quite similar to that of HeLa cells treated with PBS (Fig. S9a). Taken together, the developed Fe₃O₄@Au-PEI.Ac-PEG-FA NSs display good hemocompatibility and cytocompatibility in the studied concentration range.

In vitro cellular uptake assay and targeted MR and CT imaging of cancer cells. To verify the high affinity of the produced Fe₃O₄@Au-PEI.Ac-PEG-FA NSs to cancer cells overexpressing FAR, ICP-OES was performed to analyze the Au uptake by HeLa cells (Fig. 3a). Obviously, both HeLa-HFAR and HeLa-LFAR cells exhibit gradually enhanced Au uptake with the NS concentration. Under the same Au concentrations, the Au uptake in HeLa-HFAR cells was apparently higher than that in HeLa-LFAR cells ($p < 0.01$). This implies that the modified FA ligands onto the NSs enable specific targeting of the NSs to FAR-overexpressing cancer cells via FA-mediated pathway^{49–51}. The specific uptake of the Fe₃O₄@Au-PEI.Ac-PEG-FA NSs was further evaluated by TEM imaging (Fig. 3b,c). Clearly, HeLa-HFAR cells treated with the NSs show the remarkable distribution into the cytoplasm of the cells (Fig. 3b). In contrast, only minimal NSs were able to be detected in HeLa-LFAR cells, which is associated to the nonspecific phagocytosis or diffusion via cell walls (Fig. 3c)⁵².

MR and CT imaging were also performed to further validate the specific targeting of the NSs to HeLa-HFAR cells. T₂-weighted MR images of both HeLa-HFAR and HeLa-LFAR cells treated with the NSs become darker with the increase of Fe concentration (Fig. 3d). However, HeLa-HFAR cells show a more prominent MR signal intensity decrease under the same Fe concentrations than HeLa-LFAR cells. This was further validated by quantifying the MR signal intensity of HeLa-HFAR and HeLa-LFAR cells treated with the NSs (Fig. 3e). On the other hand, CT images and the quantitative CT values (HU) of the cells treated with the NSs (Fig. 3f,g) reveal that the CT contrast enhancement of HeLa-HFAR cells is much more obvious than that of HeLa-LFAR cells ($p < 0.05$) under the same Au concentrations, indicating that the FA renders the NSs with a targeting specificity to cancer cells that overexpress FAR. Overall, the developed Fe₃O₄@Au-PEI.Ac-PEG-FA NSs are able to be used for specific MR and CT imaging of FAR-overexpressing cancer cells *in vitro*.

In vitro photothermal ablation of cancer cells. Inspired by the high-performance photothermal property and FA-enabled targeting specificity, we used the Fe₃O₄@Au-PEI.Ac-PEG-FA NSs for PTT of cancer cells *in vitro* (Fig. 3h). Apparently, HeLa cells after treatment with the NSs without laser irradiation are quite healthy with viability comparable to those treated with PBS (control). In sharp contrast, the viability of HeLa cells after treatment with the NSs and irradiated under an 808 nm laser (1.0 W/cm²) for 5 min markedly decreases even at the Au concentration as low as 0.1 mM ($p < 0.001$). With the increase of Au concentration, the NSs exert more prominent ablation effect on cancer cells and 75.3% of HeLa cells can be killed at an Au concentration of 0.8 mM.

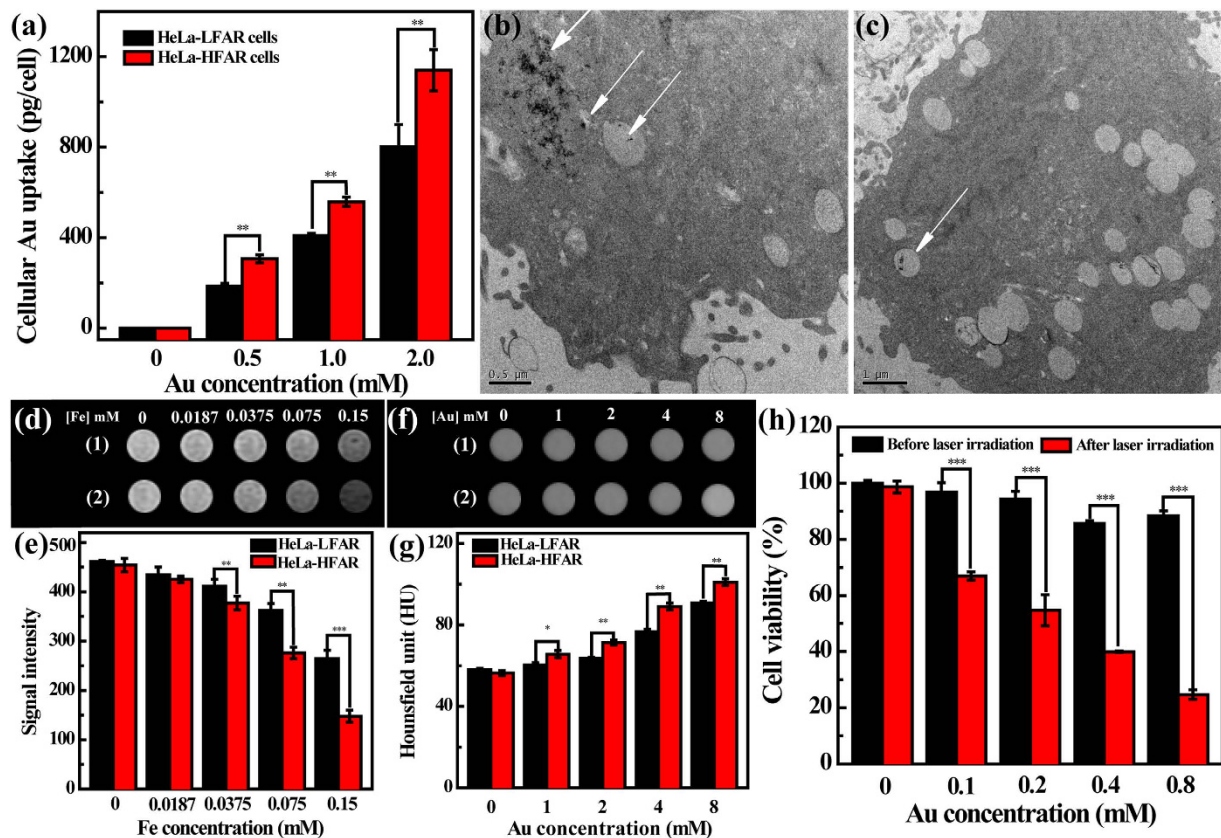


Figure 3. *In vitro* cellular uptake assay, targeted MR and CT imaging and photothermal ablation of HeLa cells. (a) The Au uptake by HeLa-HFAR and HeLa-LFAR cells after treated with the Fe_3O_4 @ Au-PEI-Ac-PEG-FA NSs at various Au concentrations for 4 h. TEM images of (b) HeLa-HFAR and (c) HeLa-LFAR cells after treated with the Fe_3O_4 @ Au-PEI-Ac-PEG-FA NSs for 4 h, respectively. (d) T_2 -weighted MR images, (e) MR signal intensity, (f) CT images, and (g) CT value of HeLa-HFAR and HeLa-LFAR cells treated with the Fe_3O_4 @ Au-PEI-Ac-PEG-FA NSs at varying Fe or Au concentrations for 6 h. (h) MTT assay of HeLa cell viability after treatment with the Fe_3O_4 @ Au-PEI-Ac-PEG-FA NSs in a given Au concentration range under an 808 nm laser irradiation for 5 min. 1 and 2 represent the HeLa-LFAR and HeLa-HFAR cells, respectively.

The PTT of cancer cells using the Fe_3O_4 @ Au-PEI-Ac-PEG-FA NSs was further investigated by cell morphology observation (Supplementary Fig. S10). Clearly, the morphologies of HeLa cells treated with PBS (Fig. S10a,f) and the NSs alone at the Au concentrations of 0.1–0.8 mM are quite healthy (Fig. S10b–e). In sharp contrast, after treatment with the NSs plus laser irradiation (Fig. S10g–j), HeLa cells are detached and rounded even at the lowest Au concentration of 0.1 mM, indicating that the cells have undergone apoptosis. The cell morphology observation results corroborate the MTT viability assay data, confirming the excellent performance of the NSs for PTT of cancer cells *in vitro*.

***In vivo* MR/CT/PA tri-mode imaging of a xenografted tumor model.** Next, the feasibility to use the Fe_3O_4 @ Au-PEI-Ac-PEG-FA NSs for tri-mode MR/CT/PA imaging of xenografted HeLa tumors *in vivo* were explored. As shown in Fig. 4a,b, the region of tumor becomes markedly dark at 0.5 h post intratumoral (IT) injection or at 6 h post intravenous (IV) injection. Quantitative MR signal intensity analysis show that the tumor MR signal intensity dramatically decreases from 256.6 to 20.1 and from 362.7 to 247.7 for IT and IV injection, respectively ($p < 0.001$) (Fig. 4c,d). This validates the use of the NSs for MR imaging of the tumors *in vivo*. To demonstrate the targeting specificity of the NSs, free FA-blocked HeLa tumor was also imaged by MR after IV injection under the same condition (Supplementary Fig. S11). Clearly, the tumor region displayed similar brightness at 6 h post IV injection to that before injection (Fig. S11a), which can be further confirmed by quantitative MR signal intensity analysis (Fig. S11b).

We then tested the potential to use the NSs for CT and PA imaging of the HeLa tumor. For CT imaging, the brightness of tumor site increases at 0.5 h post IT injection or at 6 h post IV injection (Fig. 4e,f). This can be further validated by collecting the CT value of the tumor region (Fig. 4g,h). Clearly, the CT value of tumor site significantly increases from 32.6 to 364.9 HU at 0.5 h post IT injection and from 30.4 to 43.0 HU at 6 h post IV injection, respectively ($p < 0.01$). For PA imaging, once the NSs absorb NIR laser and transform it into heat, the ambient environment can be expanded under this heat and generate an ultrasound signal. We then performed both PA and ultrasound imaging of the tumors. As shown in Fig. 5a,c, intense PA signal of tumor area can be easily visualized after IT and IV injection of NSs into tumor-bearing mice. When compared to the PA intensity of tumor

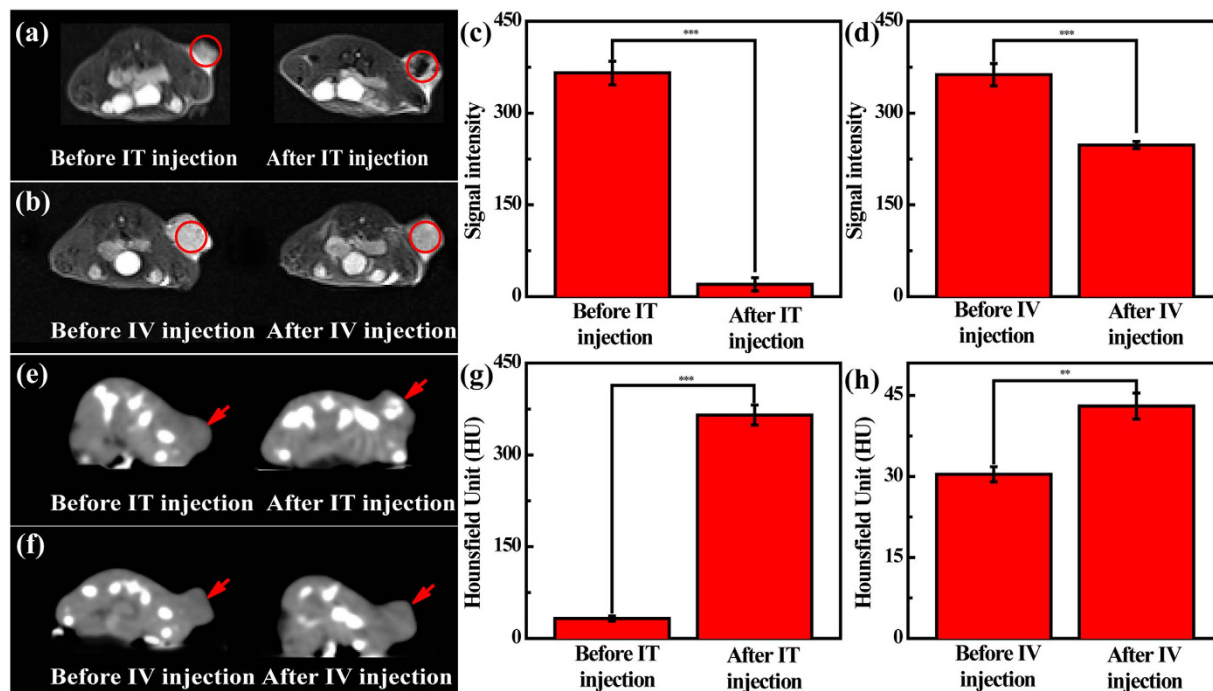


Figure 4. *In vivo* MR/CT imaging of a xenografted tumor model. (a,b) T_2 -weighted MR images, (c,d) MR signal intensity, (e,f) CT images, and (g,h) CT value of tumors before and at 0.5 h post IT (a,c,e,g) and at 6 h post IV (b,d,f,h) injection of the $Fe_3O_4@Au$ -PEI.Ac-PEG-FA NSs ([Fe] = 1.31 mM, [Au] = 70 mM, 0.1 mL in PBS).

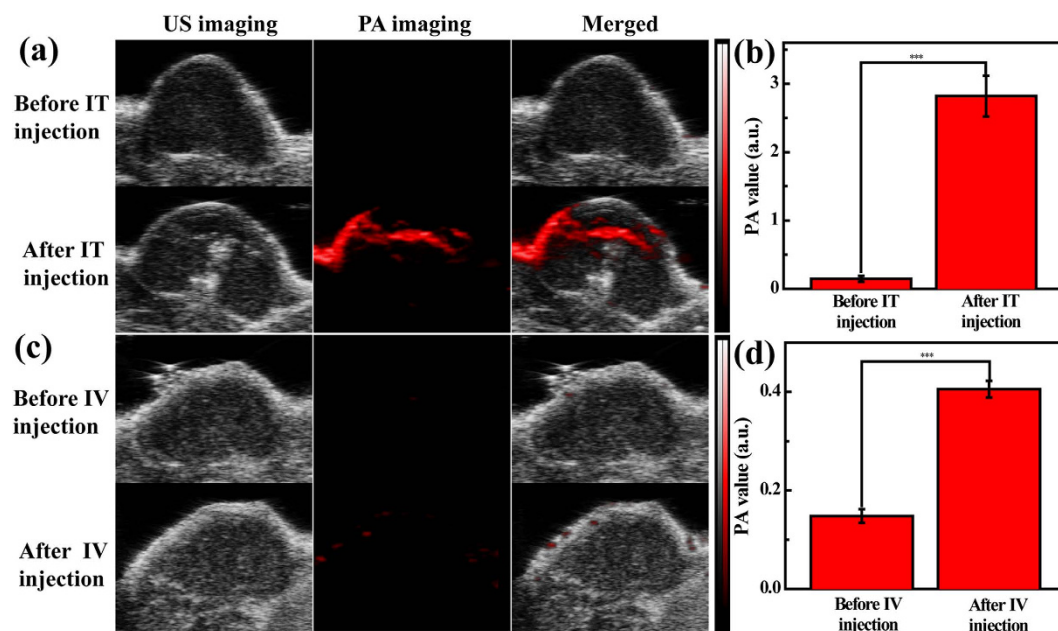


Figure 5. *In vivo* PA imaging of a xenografted tumor model. *In vivo* ultrasound/PA images (a,c) and PA value (b,d) of tumors before and at 0.5 h post IT ([Au] = 100 mM, 0.04 mL in PBS, a,b) and at 6 h post IV ([Au] = 100 mM, 0.1 mL in PBS, c,d) injection of the $Fe_3O_4@Au$ -PEI.Ac-PEG-FA NSs.

region before injection, the PA intensity is approximately 20 folds and 3 folds higher for IT injection (increase from 0.14 to 2.82) and IV injection (increase from 0.14 to 0.41), respectively ($p < 0.001$, Fig. 5b,d). The enhanced tumor MR/CT/PA imaging should be due to the modification of PEGylated FA onto the particle surfaces. On one hand (particularly for IV injection), the PEGylation modification of NSs enables them to escape from the uptake by the reticuloendothelial system (RES) and to accumulate in the tumor tissue *via* a passive targeting pathway based on enhanced permeability and retention (EPR) effect⁵³; on the other hand, with the FA-mediated active

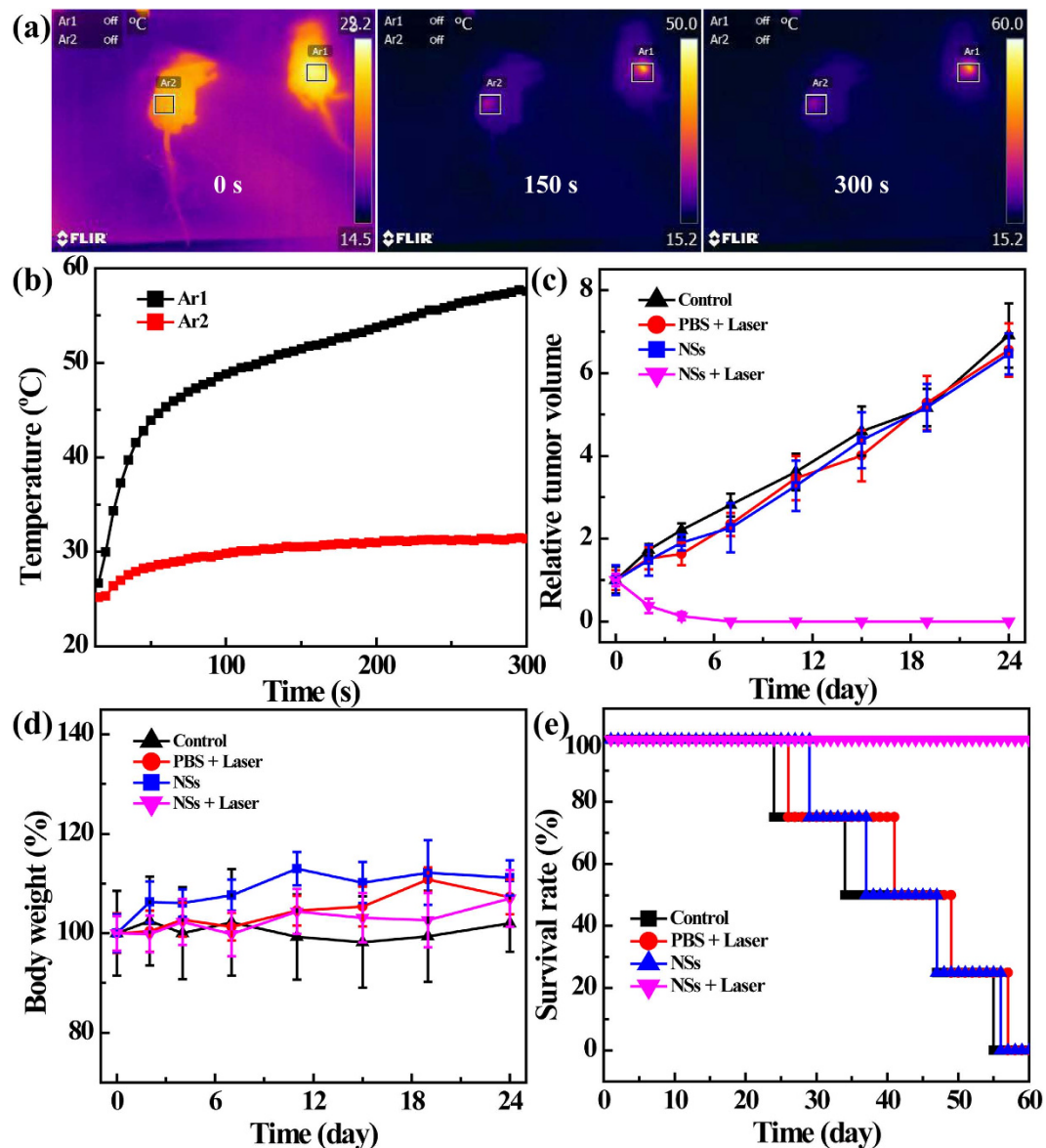


Figure 6. *In vivo* photothermal imaging and photothermal ablation of HeLa tumors. (a) Full-body photothermal images of HeLa tumor-bearing mice after IT injection with 0.1 mL PBS (control, the right mouse, indicated at region Ar2) or $\text{Fe}_3\text{O}_4@ \text{Au-PEI.Ac-PEG-FA}$ NSs dispersed in 0.1 mL PBS ($[\text{Au}] = 20 \text{ mM}$, the left mouse, indicated at region Ar1), followed by exposure to an 808 nm laser with a power density of 1.0 W/cm^2 at a time point of 0 min, 2.5 min, and 5 min, respectively. (b) The plot of temperature increase in tumor regions (Ar1 and Ar2) as a function of irradiation time. (c) The tumor volume change profiles, (d) body weight change, and (e) survival rate of tumor-bearing mice ($n = 4$) as a function of time posttreatment.

targeting pathway as demonstrated in the *in vitro* studies, the NSs are able to specifically target the tumor tissue for highly effective tumor MR/CT/PA imaging.

***In vivo* PTT of a xenografted tumor model.** Next, the potential to employ the $\text{Fe}_3\text{O}_4@ \text{Au-PEI.Ac-PEG-FA}$ NSs for thermal imaging and PTT of tumors were tested (Fig. 6). Intravital thermal imaging of mice was conducted at different laser irradiation time periods using an infrared camera. As shown in Fig. 6a,b, the temperature of Region Ar1 (administered with the NSs) rapidly increases by 24.7°C within 150 s, and by 30.8°C after 300 s of irradiation. In contrast, for Region Ar2 (administered with PBS), a subtle temperature elevation was observed and the temperature increases just approximately 5°C during the laser irradiation.

This high-temperature caused by NSs under laser irradiation is expected to ablate tumors. Next, we examined the tumor volume change of the mice after different treatments (Fig. 6c). The relative volumes of tumors at 24 days posttreatment for the groups of control (PBS), PBS + Laser, and NSs are approximately 6–7 times larger than that of the initial tumor. In sharp contrast, the treatment using NSs plus laser is able to completely ablate the tumors at 7 days postinjection of the NSs. This clearly illustrates the possibility to employ the NSs for highly efficient PTT

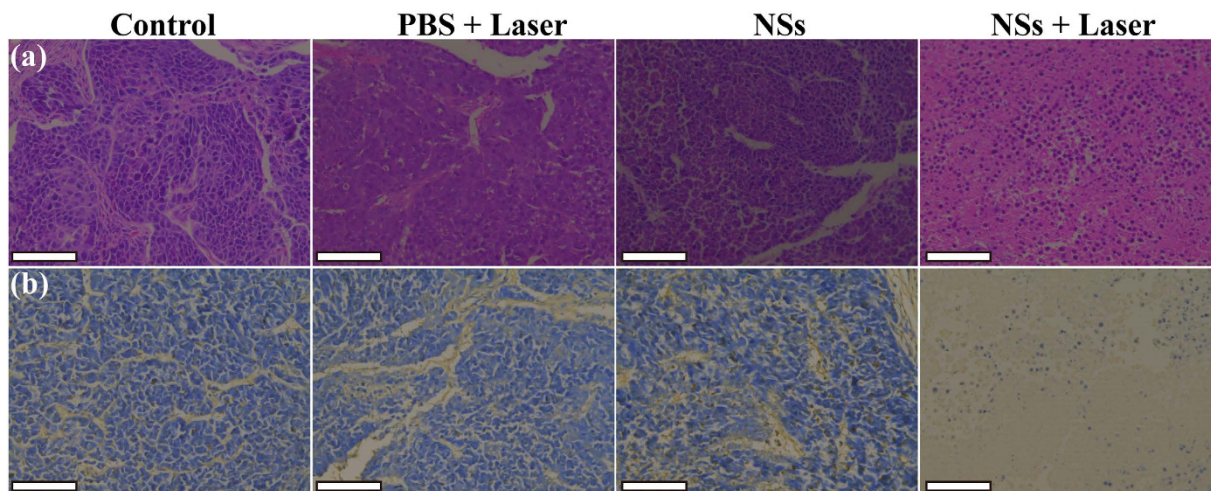


Figure 7. Histological examinations. (a) H&E and (b) TUNEL staining of tumor sections after the tumor mice were treated under different conditions. The scale bar shown in each panel of (a,b) represents 100 μm .

of tumors. The PTT efficacy of tumors can be easily visualized by taking photos of the mice (Supplementary Fig. S12). The mice in the NSs + Laser group maintain healthy at 19 days posttreatment, and the completely ablated tumor region does not seem to recur in the studied time period, suggesting the excellent PTT efficiency of the $\text{Fe}_3\text{O}_4 @ \text{Au-PEI.Ac-PEG-FA}$ NSs. In contrast, for the mice in the groups of Control, PBS + Laser, and NSs, the tumors grow bigger and bigger with the time. It should be noted that, during the experimental time period, mice with different treatments are able to maintain their body weights (Fig. 6d), suggesting that the treatments using the laser alone, the NSs alone, or the laser plus NSs are not toxic to the mice. Finally, the PTT efficacy of the tumors was evaluated by monitoring the survival rate of the mice after different treatments (Fig. 6e). Obviously, after treatment with the NSs plus laser irradiation, the mean survival rate of mice keeps 100% after 60 days. However, mice treated with PBS (Control group), PBS plus laser, and NSs alone survive with an average life-span of 40 days, 43 days, and 42 days, respectively.

Histology examinations. The PTT efficacy of tumors were further confirmed by histological examinations using H&E and TUNEL staining of harvested tumor sections (Fig. 7). H&E staining (Fig. 7a) reveals that the tumors either treated with PBS plus laser or the NSs alone exhibit normal HeLa tumor cell morphology, similar to those treated with PBS (control). But for tumors treated with the NSs plus laser, necrosis cells can be clearly seen in the whole section. Likewise, TUNEL staining (Fig. 7b) shows that only a very small amount of positive staining of apoptotic cells can be found in the sections of control, PBS + Laser, and NSs groups. In sharp contrast, after treatment with the NSs plus laser irradiation, the tumors display a huge amount of positive staining of apoptotic cells. Quantitative analysis data further reveal that the percentages of apoptotic cells in the tumors of the Control, PBS + Laser, NSs, and NSs + Laser groups are 1.5%, 3.3%, 1.3%, and 95.0%, respectively (Supplementary Fig. S13).

Discussion

Generally, $\text{Fe}_3\text{O}_4 @ \text{Au}$ CNPs could be synthesized *via* various routes and utilized for dual mode MR/CT imaging applications^{10,20,27}. On the other hand, star-shaped Au shells with strong SPR band in NIR region enable their applications in PA imaging and PTT of tumors *in vivo*¹⁸. In this work, we designed the $\text{Fe}_3\text{O}_4 @ \text{Au-PEI.Ac-PEG-FA}$ NSs with targeting specificity to FAR-expressing cancer cells for multi-modal MR/CT/PA imaging and PTT of tumors *in vivo*. Compared to our previous study utilizing hyaluronic acid as a targeting ligand³⁹, our current work aimed to expand the scope of the designed platform for theranostics of different cancer phenotypes.

Through depositing Au shell on the surface of $\text{Fe}_3\text{O}_4 @ \text{Ag}$ seeds (Supplementary Fig. S1), the $\text{Fe}_3\text{O}_4 @ \text{Au}$ core/shell NSs were formed and then successively decorated with PEI (4.8%) *via* the formation of Au-S bond and COOH-PEG-FA (7.6%) *via* the formation of amide bond (Supplementary Fig. S4). After acetylation of the remaining PEI surface amines (Supplementary Table S1), multifunctional $\text{Fe}_3\text{O}_4 @ \text{Au-PEI.Ac-PEG-FA}$ NSs were formed. The formed NSs have a slightly positive surface potential (+14.4 mV), which doesn't seem to exert any appreciable *in vivo* toxicity. This can be confirmed by monitoring the physiological status of mice after IV treatment of NSs for at least 10 days, in agreement with our previous work⁵⁴. It should be mentioned that the designed $\text{Fe}_3\text{O}_4 @ \text{Au-PEI.Ac-PEG-FA}$ NSs have a low molar ratio of Fe/Au (1:53.4). Due to the fact that we prepared the Fe_3O_4 seed NPs using a mild reduction route, the formed $\text{Fe}_3\text{O}_4 @ \text{Au}$ core/shell NSs have a r_2 relaxivity ($549.07 \text{ mM}^{-1} \text{ s}^{-1}$) 3.8 times higher than the $\text{Fe}_3\text{O}_4 @ \text{Au}$ core/shell NSs ($144.39 \text{ mM}^{-1} \text{ s}^{-1}$) reported in our previous work³⁹. With the higher Au content than other $\text{Fe}_3\text{O}_4 @ \text{Au}$ NPs^{27,55} and non-compromised MR imaging sensitivity, the designed NSs should be able to be used for sensitive MR and CT imaging. Our results reveal that the NSs display good MR relaxometry, X-ray attenuation, PA property and photothermal performance (Fig. 2), which is due to the co-existence of Fe_3O_4 core and star-shaped Au shell. The η of the NSs (88.9%, Supplementary Fig. S7) is much higher than that of other major PTT agents reported in the literature^{43–46}, which is likely ascribed to

the particle's volume, structure, and shape⁵⁶. The FA modification of the particles rendered the NSs with specific affinity to FAR-overexpressing cancer cells *in vitro* (Fig. 3a–g) and the xenografted tumor model *in vivo* (Fig. 4b,d and Supplementary Fig. S11). Hence the NSs hold great promise to be used as a nanoprobe for specific MR/CT/PA imaging of a FAR-expressing tumor model *in vivo* after either IT or IV injection (Figs 4 and 5). The tumor MR/CT/PA signal intensities after IV injection of the NSs are poorer than those of the corresponding imaging signals after IT injection of the NSs. This should be due to the fact that much less NSs were accumulated in tumors *via* IV injection than *via* IT injection. Additionally, the NIR-absorption feature of NSs affords their uses for efficient PTT of cancer cells *in vitro* and the tumor model *in vivo* (Figs 3h and 6). It should be mentioned that due to the fact that NPs with a size of 50–300 nm regardless of surface modification of targeting ligands have a significant accumulation in the tumor region after IT injection^{33,44,57}, we used IT injection route to evaluate the PTT efficacy of the tumors *in vivo* using the designed NSs.

To conclude, we presented a novel route to generating Fe₃O₄@Au-PEI.Ac-PEG-FA NSs that can be used as a unique platform for multi-mode MR/CT/PA imaging and PTT of tumors. *Via* the integration of mild reduction route, seed-mediated growth method, and PEI-mediated conjugation, multifunctional Fe₃O₄@Au-PEI.Ac-PEG-FA NSs are able to be formed. The designed NSs possess excellent colloidal stability, good hemocompatibility/cytocompatibility, ultrahigh τ_2 relaxivity, good X-ray attenuation and PA property, and strong NIR absorption feature. These properties afford their uses as a theranostic nanoprobe for multi-mode imaging-guided PTT of tumors. Furthermore, the synthesized FA-modified Fe₃O₄@Au core/shell NSs are likely to be used for theranostics of different types of cancer for further translational medicine applications.

Methods

Materials. All chemicals and materials were from commercial resources and used as received. Details can be seen in Supplementary Information.

Characterization techniques. The intermediate products and Fe₃O₄@Au-PEI.Ac-PEG-FA NSs were thoroughly characterized *via* hydrodynamic size and zeta potential measurements, ¹H NMR spectroscopy, thermal gravimetric analysis (TGA), UV-vis spectroscopy, transmission electron microscopy (TEM), Leeman Prodigy inductively coupled plasma-optical emission spectroscopy (ICP-OES), T₂ relaxometry measurements, MR/CT/PA phantom studies, and photothermal performance.

Preparation of Fe₃O₄@Au NSs. Fe₃O₄/Ag seed particles were prepared by a protocol adopted from the literature^{10,40,41,58}. To grow Au NSs onto the surface of Fe₃O₄ NPs, an Au growth solution with three different proportions of reagents (AgNO₃, AA, and HAuCl₄) was used. Only the mixture that changed to blue and exhibited strong NIR-absorption in the UV-vis-NIR spectrum was regarded as the best option of Au growth solution for the formation of Fe₃O₄@Au NSs.

Synthesis of Fe₃O₄@Au-PEI.Ac-PEG-FA NSs. Firstly, PEI-SH and COOH-PEG-FA were synthesized using protocols illustrated in the literature^{19,39,49,59}. Thereafter, the above Fe₃O₄@Au NSs were successively modified with PEI-SH *via* the formation of Au-S bond and COOH-PEG-FA *via* the formation amido linkage. After neutralizing the remaining PEI amines, the Fe₃O₄@Au-PEI.Ac-PEG-FA NSs were obtained.

Hemolysis and cytotoxicity assay. Hemolysis assay was performed by exposing human red blood cells (HRBCs) to a phosphate buffered saline (PBS) solution containing Fe₃O₄@Au-PEI.Ac-PEG-FA NSs in the Au concentration range of 0–4 mM for 2 h at room temperature. HeLa cells were routinely cultured and passaged in 25 cm² plates at 37 °C and 5% CO₂ in regular FA-free DMEM with 10% FBS, 1% penicillin/streptomycin. HeLa cells cultured in FA-free medium expressed high-level FAR (denoted as HeLa-HFAR cells)^{60,61}, while HeLa cells grown in the DMEM containing 2.5 μM free FA for 24 h or longer expressed low-level FAR (denoted as HeLa-LFAR). Without specific statement, the term of “HeLa cells” is always deemed to be “HeLa-HFAR cells”. Cytotoxicity assay was conducted by culturing HeLa cells with fresh DMEM containing Fe₃O₄@Au-PEI.Ac-PEG-FA NSs in the tested Au concentration range (0–2 mM) for 24 h. MTT assay and cell morphology observation were used to quantitatively and qualitatively assess the cell viability.

***In vitro* specific cellular uptake assay.** After incubation of both HeLa-HFAR and HeLa-LFAR with Fe₃O₄@Au-PEI.Ac-PEG-FA NSs for 4–6 h, ICP-OES, TEM, MR imaging, and CT imaging were performed to determine or demonstrate the specific uptake of the NSs by HeLa-HFAR cells.

***In vitro* photothermal ablation of HeLa cells.** After cultivation with DMEM containing PBS (control) or Fe₃O₄@Au-PEI.Ac-PEG-FA NSs in the studied Au concentration range for 6 h, adherent HeLa cells were then rinsed with PBS and subjected to laser irradiation. MTT viability assay and cell morphology observation were then performed to quantitatively and qualitatively assess the cell viability, respectively.

***In vivo* MR/CT/PA tri-modal imaging of a xenografted tumor model.** All animal experiments were conducted in compliance with institutional guidelines and the policy of the National Ministry of Health, and were approved by the Institutional Animal Care and Use Committee of Zhongshan Hospital, Fudan University. A PBS solution (0.1 mL) containing the Fe₃O₄@Au-PEI.Ac-PEG-FA NSs ([Fe] = 1.31 mM) was delivered into each tumor-bearing mouse *via* an intravenous (IV) or intratumoral (IT) injection route. For MR imaging, tumor 2D MR images were collected before and at 0.5 h post IT injection or at 6 h post IV injection of the NSs by using a Sigma HDxt superconductor clinical MR system (1.5 T). To verify the targeting specificity of NSs to FAR-expressing HeLa tumor, IV injection of free FA was first performed to block the FAR expression, followed by

IV injection of the NSs. Tumor CT and PA imaging were further carried out with a GE LightSpeed VCT imaging system and the Vevo LAZR PA Imaging System, respectively.

In vivo photothermal ablation of HeLa tumors. Intravital thermal imaging of HeLa tumor-bearing mice was first conducted at different laser irradiation time periods using an infrared camera. For PTT of tumors, the mice were randomly allocated into four groups and subjected to different treatments: Control group (without any treatment), PBS + Laser group (PBS with laser), NSs group (NSs without laser), and NSs + Laser group (NSs with laser). Thereafter, the size of the tumors, body weight and tumor volume were recorded at different time points. More experimental details can be found in Supplementary information.

References

- Gambhir, S. S. Molecular imaging of cancer with positron emission tomography. *Nat. Rev. Cancer* **2**, 683–693 (2002).
- Weissleder, R. Molecular imaging in cancer. *Science* **312**, 1168–1171 (2006).
- Yu, M. *et al.* Noninvasive staging of kidney dysfunction enabled by renal-clearable luminescent gold nanoparticles. *Angew. Chem. Int. Ed.* **55**, 2787–2791 (2016).
- Keren, S. *et al.* Noninvasive molecular imaging of small living subjects using raman spectroscopy. *Proc. Natl. Acad. Sci. USA* **105**, 5844–5849 (2008).
- Bardhan, R. *et al.* Nanoshells with targeted simultaneous enhancement of magnetic and optical imaging and photothermal therapeutic response. *Adv. Funct. Mater.* **19**, 3901–3909 (2009).
- Lee, D.-E. *et al.* Multifunctional nanoparticles for multimodal imaging and theragnosis. *Chem. Soc. Rev.* **41**, 2656–2672 (2012).
- Huh, Y.-M. *et al.* In vivo magnetic resonance detection of cancer by using multifunctional magnetic nanocrystals. *J. Am. Chem. Soc.* **127**, 12387–12391 (2005).
- Shi, X. *et al.* Dendrimer-functionalized shell-crosslinked iron oxide nanoparticles for in-vivo magnetic resonance imaging of tumors. *Adv. Mater.* **20**, 1671–1678 (2008).
- Hu, Y., Li, J., Shen, M. & Shi, X. Formation of multifunctional Fe₃O₄/Au composite nanoparticles for dual-mode MR/CT imaging applications. *Chin. Phys. B* **23**, 78704–78711 (2014).
- Hu, Y. *et al.* Facile synthesis of RGD peptide-modified iron oxide nanoparticles with ultrahigh relaxivity for targeted MR imaging of tumors. *Biomater. Sci.* **3**, 721–732 (2015).
- Jakhmola, A., Anton, N. & Vandamme, T. F. Inorganic nanoparticles based contrast agents for X-ray computed tomography. *Adv. Healthcare Mater.* **1**, 413–431 (2012).
- Lusic, H. & Grinstaff, M. W. X-ray-computed tomography contrast agents. *Chem. Rev.* **113**, 1641–1666 (2013).
- Nie, L. *et al.* In vivo volumetric photoacoustic molecular angiography and therapeutic monitoring with targeted plasmonic nanostars. *Small* **10**, 1585–1593 (2014).
- Dinish, U. S. *et al.* Single molecule with dual function on nanogold: Biofunctionalized construct for in vivo photoacoustic imaging and SERS biosensing. *Adv. Funct. Mater.* **25**, 2316–2325 (2015).
- Huang, X., El-Sayed, I. H., Qian, W. & El-Sayed, M. A. Cancer cell imaging and photothermal therapy in the near-infrared region by using gold nanorods. *J. Am. Chem. Soc.* **128**, 2115–2120 (2006).
- Yang, K. *et al.* Graphene in mice: Ultrahigh in vivo tumor uptake and efficient photothermal therapy. *Nano Lett.* **10**, 3318–3323 (2010).
- Wang, S. *et al.* A facile one-pot synthesis of a two-dimensional MoS₂/Bi₂S₃ composite theranostic nanosystem for multi-modality tumor imaging and therapy. *Adv. Mater.* **27**, 2775–2782 (2015).
- Huang, J. *et al.* Rational design and synthesis gamma Fe₂O₃@ Au magnetic gold nanoflowers for efficient cancer theranostics. *Adv. Mater.* **27**, 5049–+ (2015).
- Chen, Q. *et al.* Targeted CT/MR dual mode imaging of tumors using multifunctional dendrimer-entrapped gold nanoparticles. *Biomaterials* **34**, 5200–5209 (2013).
- Zhu, J. *et al.* Synthesis of Au-Fe₃O₄ heterostructured nanoparticles for in vivo computed tomography and magnetic resonance dual model imaging. *Nanoscale* **6**, 199–202 (2014).
- Li, C. *et al.* Gold-coated Fe₃O₄ nanoroses with five unique functions for cancer cell targeting, imaging, and therapy. *Adv. Funct. Mater.* **24**, 1772–1780 (2013).
- Li, J. *et al.* Hyaluronic acid-modified hydrothermally synthesized iron oxide nanoparticles for targeted tumor MR imaging. *Biomaterials* **35**, 3666–3677 (2014).
- Cao, Y. *et al.* Targeted CT imaging of human hepatocellular carcinoma using low-generation dendrimer-entrapped gold nanoparticles modified with lactobionic acid. *J. Mater. Chem. B* **3**, 286–295 (2015).
- Peng, C. *et al.* PEGylated dendrimer-entrapped gold nanoparticles for in vivo blood pool and tumor imaging by computed tomography. *Biomaterials* **33**, 1107–1119 (2012).
- Cai, H. *et al.* Facile assembly of Fe₃O₄@ Au nanocomposite particles for dual mode magnetic resonance and computed tomography imaging applications. *J. Mater. Chem.* **22**, 15110–15120 (2012).
- Zhao, H. Y. *et al.* Synthesis and application of strawberry-like Fe₃O₄-Au nanoparticles as CT-MR dual-modality contrast agents in accurate detection of the progressive liver disease. *Biomaterials* **51**, 194–207 (2015).
- Cai, H. *et al.* Dendrimer-assisted formation of Fe₃O₄/Au nanocomposite particles for targeted dual mode CT/MR imaging of tumors. *Small* **11**, 4584–4593 (2015).
- Yuan, H., Fales, A. M. & Vo-Dinh, T. TAT peptide-functionalized gold nanostars: Enhanced intracellular delivery and efficient NIR photothermal therapy using ultralow irradiance. *J. Am. Chem. Soc.* **134**, 11358–11361 (2012).
- Wang, S. *et al.* Single continuous wave laser induced photodynamic/plasmonic photothermal therapy using photosensitizer-functionalized gold nanostars. *Adv. Mater.* **25**, 3055–3061 (2013).
- Rodriguez-Lorenzo, L., de la Rica, R., Alvarez-Puebla, R. A., Liz-Marzan, L. M. & Stevens, M. M. Plasmonic nanosensors with inverse sensitivity by means of enzyme-guided crystal growth. *Nat. Mater.* **11**, 604–607 (2012).
- Li, J., Day, D. & Gu, M. Ultra-low energy threshold for cancer photothermal therapy using transferrin-conjugated gold nanorods. *Adv. Mater.* **20**, 3866–3871 (2008).
- Seo, S.-H. *et al.* NIR-light-induced surface-enhanced raman scattering for selection and photothermal/photodynamic therapy of cancer cells using methylene blue-embedded gold nanorod @ SiO₂ nanocomposites. *Biomaterials* **35**, 3309–3318 (2014).
- Huang, X., Neretina, S. & El-Sayed, M. A. Gold nanorods: From synthesis and properties to biological and biomedical applications. *Adv. Mater.* **21**, 4880–4910 (2009).
- Li, S. *et al.* The facile synthesis of hollow Au nanoflowers for synergistic chemo-photothermal cancer therapy. *Chem. Commun.* **51**, 14338–14341 (2015).
- Gao, L. *et al.* Hypocrellin-loaded gold nanocages with high two-photon efficiency for photothermal/photodynamic cancer therapy in vitro. *ACS Nano* **6**, 8030–8040 (2012).
- Wang, H. *et al.* Facile preparation of gold nanocages and hollow gold nanospheres via solvent thermal treatment and their surface plasmon resonance and photothermal properties. *J. Colloid Interface Sci.* **440**, 236–244 (2015).

37. Kennedy, L. C. *et al.* A new era for cancer treatment: Gold-nanoparticle-mediated thermal therapies. *Small* **7**, 169–183 (2011).
38. Kim, J. *et al.* Designed fabrication of multifunctional magnetic gold nanoshells and their application to magnetic resonance imaging and photothermal therapy. *Angew. Chem., Int. Ed.* **45**, 7754–7758 (2006).
39. Li, J. *et al.* Hyaluronic acid-modified Fe₃O₄@Au core/shell nanostars for multimodal imaging and photothermal therapy of tumors. *Biomaterials* **38**, 10–21 (2015).
40. Sanchez-Gaytan, B. L. & Park, S.-J. Spiky gold nanoshells. *Langmuir* **26**, 19170–19174 (2010).
41. Cheraghipour, E., Javadpour, S. & Mehdizadeh, A. R. Citrate capped superparamagnetic iron oxide nanoparticles used for hyperthermia therapy. *J. Biomed. Sci. Eng.* **5**, 715–719 (2012).
42. Zhou, B. *et al.* Synthesis and characterization of PEGylated polyethylenimine-entrapped gold nanoparticles for blood pool and tumor CT imaging. *ACS Appl. Mater. Interfaces* **6**, 17190–17199 (2014).
43. Bhana, S. *et al.* Near-infrared-absorbing gold nanopopcorns with iron oxide cluster core for magnetically amplified photothermal and photodynamic cancer therapy. *ACS Appl. Mater. Interfaces* **7**, 11637–11647 (2015).
44. Tian, Q. *et al.* Hydrophilic Cu₉S₅ nanocrystals: A photothermal agent with a 25.7% heat conversion efficiency for photothermal ablation of cancer cells *in vivo*. *ACS Nano* **5**, 9761–9771 (2011).
45. Cole, J. R., Mirin, N. A., Knight, M. W., Goodrich, G. P. & Halas, N. J. Photothermal efficiencies of nanoshells and nanorods for clinical therapeutic applications. *J. Phys. Chem. C* **113**, 12090–12094 (2009).
46. Huang, P. *et al.* Biodegradable gold nanovesicles with an ultrastrong plasmonic coupling effect for photoacoustic imaging and photothermal therapy. *Angew. Chem., Int. Ed.* **52**, 13958–13964 (2013).
47. Shen, M. *et al.* Facile one-pot preparation, surface functionalization, and toxicity assay of APTS-coated iron oxide nanoparticles. *Nanotechnology* **23**, 105601 (2012).
48. Peng, C. *et al.* Facile formation of dendrimer-stabilized gold nanoparticles modified with diatrizoic acid for enhanced computed tomography imaging applications. *Nanoscale* **4**, 6768–6778 (2012).
49. Zhu, J. *et al.* Targeted cancer theranostics using alpha-tocopheryl succinate-conjugated multifunctional dendrimer-entrapped gold nanoparticles. *Biomaterials* **35**, 7635–7646 (2014).
50. Liu, H. *et al.* Facile formation of folic acid-modified dendrimer-stabilized gold-silver alloy nanoparticles for potential cellular computed tomography imaging applications. *Analyst* **138**, 1979–1987 (2013).
51. Zheng, Y. *et al.* Multifunctional dendrimers modified with alpha-tocopheryl succinate for targeted cancer therapy. *Medchemcomm* **5**, 879–885 (2014).
52. Wang, H. *et al.* Computed tomography imaging of cancer cells using acetylated dendrimer-entrapped gold nanoparticles. *Biomaterials* **32**, 2979–2988 (2011).
53. Liu, H. *et al.* Synthesis of PEGylated low generation dendrimer-entrapped gold nanoparticles for CT imaging applications. *Nanoscale* **6**, 4521–4526 (2014).
54. Li, J. *et al.* Facile synthesis of folic acid-functionalized iron oxide nanoparticles with ultrahigh relaxivity for targeted tumor MR imaging. *J. Mater. Chem. B* **3**, 5720–5730 (2015).
55. Hu, Y. *et al.* Facile synthesis of hyaluronic acid-modified Fe₃O₄/Au composite nanoparticles for targeted dual mode MR/CT imaging of tumors. *J. Mater. Chem. B* **3**, 9098–9108 (2015).
56. Chen, H. *et al.* Understanding the photothermal conversion efficiency of gold nanocrystals. *Small* **6**, 2272–2280 (2010).
57. Farokhzad, O. C. *et al.* Targeted nanoparticle-aptamer bioconjugates for cancer chemotherapy *in vivo*. *Proc. Natl. Acad. Sci. USA* **103**, 6315–6320 (2006).
58. Bhana, S., Rai, B. K., Mishra, S. R., Wang, Y. & Huang, X. Synthesis and properties of near infrared-absorbing magnetic-optical nanopins. *Nanoscale* **4**, 4939–4942 (2012).
59. Pan, B. *et al.* Controlled self-assembly of thiol-terminated poly(amidoamine) dendrimer and gold nanoparticles. *Colloids Surf. A* **259**, 89–94 (2005).
60. Zheng, X. *et al.* mRNA instability in the nucleus due to a novel open reading frame element is a major determinant of the narrow tissue specificity of folate receptor alpha. *Mol. Cell. Biol.* **23**, 2202–2212 (2003).
61. Sun, C., Sze, R. & Zhang, M. Folic acid-PEG conjugated superparamagnetic nanoparticles for targeted cellular uptake and detection by MRI. *J. Biomed. Mater. Res., Part A* **78A**, 550–557 (2006).

Acknowledgements

Financial support from the National Natural Science Foundation of China (21273032 and 81341050), the Sino-German Center for Research Promotion (GZ899), and the Program for Professor of Special Appointment (Eastern Scholar) at Shanghai Institutions of Higher Learning was greatly acknowledged. M. Shen thanks the financial support from the Science and Technology Commission of Shanghai Municipality (15520711400) and the Fundamental Research Funds for the Central Universities. Y. Hu. thanks the Innovation Funds of Donghua University Master Dissertation of Excellence (EG2015021).

Author Contributions

X.S., M.S. and X.W. contributed to the design of the experiment, analysis of the data and writing the manuscript. Y.H., R.W. and S.W. performed the experiments and data analysis, and wrote the draft of the manuscript. L.D., J.L. and Y.L. assisted with some of the experiments. Y.H., R.W. and S.W. contributed equally to this work.

Additional Information

Supplementary information accompanies this paper at <http://www.nature.com/srep>

Competing financial interests: The authors declare no competing financial interests.

How to cite this article: Hu, Y. *et al.* Multifunctional Fe₃O₄@Au core/shell nanostars: a unique platform for multimode imaging and photothermal therapy of tumors. *Sci. Rep.* **6**, 28325; doi: 10.1038/srep28325 (2016).



This work is licensed under a Creative Commons Attribution 4.0 International License. The images or other third party material in this article are included in the article's Creative Commons license, unless indicated otherwise in the credit line; if the material is not included under the Creative Commons license, users will need to obtain permission from the license holder to reproduce the material. To view a copy of this license, visit <http://creativecommons.org/licenses/by/4.0/>